Remarkable catalytic properties of rare-earth doped nickel ferrites synthesized by sol-gel auto-combustion with maleic acid as fuel for CWPO of dyes

Petrisor Samoila [a,*], Corneliu Cojocaru [a], Liviu Sacarescu [a], Petronela Pascariu Dorneanu [a], Andrei-Adrian Domocos [b], Aurelian Rotaru [c]

[a] "Petru Poni" Institute of Macromolecular Chemistry, Aleea Grigore Ghica Voda 41 A 700487 Iasi, Romania
[b] "Alexandru Ioan Cuza" University, Departament of Physics, 11, Carol I Boulevard, 700506 Iasi, Romania
[c] "Stefan Cel Mare" University, Faculty of Electrical Engineering & Computer Science, 13Universitatii Street, 720229 Suceava, Romania

ARTICLE INFO

ABSTRACT

$NiFe_{1.98}RE_{0.02}O_4$ (where RE = La, Sm, Gd and Dy) spinel ferrites were synthesized by sol–gel autocombustion method using maleic acid as fuel. The effect of rare-earth cations (RE) doping on structural, magnetic and catalytic properties of nickel ferrite is reported. XRD and FT-IR analysis revealed the successful insertion of the rare-earth cations into the spinel matrix in all samples. We observed a decreasing of crystallite and particle sizes (estimated from XRD patterns and TEM micrographs, respectively) as well as the magnetization value in the presence of lanthanide ions into the spinel structure. Additionally, these ferrites were employed as heterogeneous catalysts for catalytic wet hydrogen peroxide oxidation (CWPO) of Orange II azo-dye. The color removal efficiency was boosted from 30.6% for undoped nickel ferrite to 90.6% for the lanthanum doped nickel ferrite, after only 15 min of reaction. The decolorization of Orange II solution followed the pseudo-first-order kinetics and was achieved via decay reaction as demonstrated by Langmuir-Hinshelwood model. The remarkable increase in catalytic performance of doped nickel ferrites with a very small amount of rare-earth cations was correlated with the size factor, expressed as the ratio between particle and crystallite size. The desirability function approach enabled to identify the optimal material ($NiFe_{1.98}La_{0.02}O_4$) with the best catalytic performance; the smallest size factor and appropriate magnetic properties.

© 2016 Elsevier B.V. All rights reserved.

1. Introduction

The pollution of water resources by large quantities of aqueous organic effluents, especially phenolic compounds and azo-dyes, generated from diverse industries such as petrochemical, pharmaceutical, chemical, textile, cosmetics or agro-alimentary has a negative environmental impact, affecting the quality of drinking water for the next generation [1,2]. The increasing strict regulations for the protection of environment are imposing lower discharge limits of toxic and potentially hazardous pollutants that are difficult to satisfy with the conventional technologies [1]. The current wastewater treatment methods based on biological, thermal, and physicochemical processes have limitations in terms of applicability, effectiveness and costs [3]. Therefore, the development of new and more efficient systems for wastewater treatment represents a great challenge for the researchers.

In this context, the Advanced Oxidation Processes (AOPs) are postulated as an attractive alternative for treating wastewater containing organic pollutants [4,5]. Usually, the AOPs procedures involve the generation of nonselective and extremely reactive hydroxyl radical ($HO^\bullet$) in the reaction medium, which is one of the most powerful oxidation agents due to its high oxidation potential ($E^0 = 2.8$ V) [4,6]. The classification of advanced oxidation processes in Fenton, photo-Fenton, ozonation, photocatalysis, catalytic wet oxidation, etc. is based on the ways in which $HO\bullet$ radicals are generated from different sources (H_2O, O_2, H_2O_2, O_3) [7–9]. The most common sources of hydroxyl radicals are the reactions of hydrogen peroxide with the Fenton or Fenton-like reagents at room temperature [4,10]. Note that, when Fenton systems are used at

* Corresponding author.
 E-mail addresses: samoila.petrisor@icmpp.ro, samoila.petrisor@yahoo.com (P. Samoila).

temperature higher than the room temperature, the processes are called catalytic wet hydrogen peroxide oxidation (CWPO) [4].

Heterogeneous CWPO is extremely attractive, among various AOPs techniques, enabling the complete mineralization of refractory organic pollutants into carbon dioxide, water and other innocuous inorganic compounds [3]. Usually, iron oxides such as magnetite (Fe_3O_4), maghemite (γFe_2O_3) and hematite (αFe_2O_3) are successfully used as heterogeneous WPO catalysts [11]. However, the development of new iron containing poly-metallic oxides with enhanced activity in CWHPO technologies is of great interest [3,4,10,12,13].

The use of other iron-based materials, such as spinel ferrites, for the catalytic degradation of organic pollutants, represents a promising alternative to achieve catalytic performances more interesting then the single metal oxide component [5,11–14]. In these cases, catalysts might be easily recovered from the reaction environment because of their magnetic properties and reused for several runs [8,13]. Despite encouraging results achieved, further systematic research work is required in order to improve the catalytic activity of the spinel ferrites. Catalytic performances of spinel ferrites are strongly influenced by various factors like chemical composition; crystallite and particle size; as well as microstructural characteristics [15]. These factors could be fine-tuned by selecting a particular route of material synthesis or an appropriate chemical composition.

Recent studies reveal a good potential of the use of rare-earth oxides and rare-earth containing polymetallic oxides for organic pollutants degradation [16–23]. In this respect, the investigation of the influence of rare-earth doping on spinel ferrites characteristics deserves special attention. It was observed that structural parameters, the perturbation occurring in the $Fe^{3+}-O^{2-}-Fe^{3+}$ bonds (the rare earth cations are bulky), particle sizes, magnetic and catalytic properties are strongly influenced by the presence of very small amounts of Dy and Gd cations in the structure of the Ni–Zn and Ni–Mn–Cr ferrites, respectively, making these kind of materials potential candidates for CWPO applications [15,24]. Nevertheless, careful survey of the literature reveals only one study reporting the enhanced catalytic activity of ferrite nanoparticles doped with rare-earth ions in CWPO of organic pollutants [25]. Note that, the insertion of rare-earth cations into the spinel matrix is difficult because of their larger ionic radii [24]. Among the synthesis methods usually employed for the rare-earth doped spinel ferrites (solid-state reaction, coprecipitation or hydrothermal) the sol-gel autocombustion is an attractive way to obtain nanocrystalline mixed oxides. This method is extensively used because of its specific characteristics like: use the chemical energy instead of the electric energy, simple synthesis setup, easy component adjustment, rapid synthesis, and ease of scale up. The sol-gel autocombustion became a reference synthesis procedure for preparation of catalytic materials [26]. The selection of the fuel agent for this kind of synthesis is essential. Thus, in a previous study we showed that from four different fuels (urea, cellulose, citric and tartaric acids) used for the synthesis of Dy substituted Ni-Zn ferrite, only cellulose, citric acid and tartaric acid led to the dissolution of dysprosium cations into spinel structure and only citric acid and cellulose lead to pure spinel phase [15].

In this work, at the first time, we used maleic acid as the combustion agent to dope the nickel ferrite with bulky cations like La^{3+}, Sm^{3+}, Gd^{3+} and Dy^{3+}. It is important to note that, only two papers discussing this carboxylic acid as a combustion agent were reported, and both presenting the preparation of some hexagonal ferrites [27,28]. To the best of our knowledge, so far, no study was reported dealing with maleic acid as fuel agent for the synthesis of any spinel ferrites. Likewise, for the first time, we used rare-earth doped spinel ferrites as catalysts for CWPO of the Orange II azo-dye, which was chosen as the model pollutant.

2. Experimental

2.1. Catalysts preparation

Nanoparticles of Ni ferrite doped with rare earth (RE) cations like La, Sm, Gd and Dy with formula $NiFe_{1.98}RE_{0.02}O_4$ were obtained by sol-gel autocombustion method using maleic acid as fuel. Likewise, the undoped $NiFe_2O_4$ ferrite was prepared for comparison purposes. Analytical reagent graded nickel nitrate [$Ni(NO_3)_2 \cdot 6H_2O$], iron nitrate [$Fe(NO_3)_3 \cdot 9H_2O$], lanthanum nitrate [$La(NO_3)_3 \cdot 6H_2O$], samarium nitrate [$Sm(NO_3)_3 \cdot 6H_2O$], gadolinium nitrate [$Gd(NO_3)_3 \cdot 6H_2O$], and maleic anhydride [$C_4H_2O_3$] were used to prepare the ferrite samples, as purchased from Sigma-Aldrich. Dysprosium nitrate solution 1 M was obtained in situ from Dy_2O_3 and nitric acid 20% solution. First, the metal nitrate solutions were mixed in stoichiometric proportions. Second, a solution of maleic acid was mixed with each sample of metal nitrates mixture into 1:1 molar ratio of fuel agent to cations. The mixed solutions were heated at 80 °C on a water bath, under continuous stirring, until a viscous gel was formed. Consequently, the gel was gradually heated at 350 °C on a sand bath, until the self-ignition was clearly observed and a dark powder was formed. The obtained powders were thermal treated in three steps: pre-sinterization at 500 °C/5 h, and sinterization at 700 °C/5 h and at 900 °C/7 h, respectively.

The obtained materials were denoted N700, NL700, NS700, NG700, ND700 and N900, NL900, NS900, NG900, ND900, respectively, indicating the rare-earth cation employed and the annealing temperature (i.e. L = La, S = Sm, G = Gd, D = Dy, 700 = 700 °C and 900 = 900 °C).

2.2. Catalysts characterization

Structural characterization of the spinel ferrite powder heated at 700 °C and at 900 °C was performed by recording the powder X-ray diffraction (XRD) patterns using a Shimadzu LabX 6000 diffractometer equipped with graphite monochromator and CuKα ($\lambda = 0.15406$ nm) radiation. The powders were scanned in the range 20–80° (2θ) with a scanning rate of 0.02°/s.

The formation of spinel-type phase at 700 °C and at 900 °C was monitored by means of infrared spectroscopy using a Bruker Vertex 70 FTIR spectrometer at room temperature with a resolution of 2 cm^{-1} (KBr pellets technique). The spectra were registered in transmission mode in the range of 350–900 cm^{-1}.

The morphology, microstructure and chemical composition of ferrite samples annealed at 900 °C were investigated using Hitachi High-Tech HT7700 Transmission Electron Microscope (TEM) equipped with a Bruker XFlash 6 energy dispersive X-ray (EDS) detector, operated in high contrast mode at 120 kV accelerating voltage. Samples were prepared by dispersion of the nanoparticles in ethanol, ultrasonication for 1 min, drop casting on carbon coated copper grids (300 mesh, Ted Pella) and drying in vacuum at 50 °C. The particle size distribution and the average particle sizes were determined using ImageJ software, by measuring at least 100 grains for each studied material from at least six different micrographs.

Magnetic measurements for the materials sintered at 900 °C were performed using an MPMS3 (7T) SQUID magnetometer, at room temperature (300 K), in DC mode, under an applied magnetic field of 4000 Oe. Before each measurement, the sample was demagnetized in AF (alternating field).
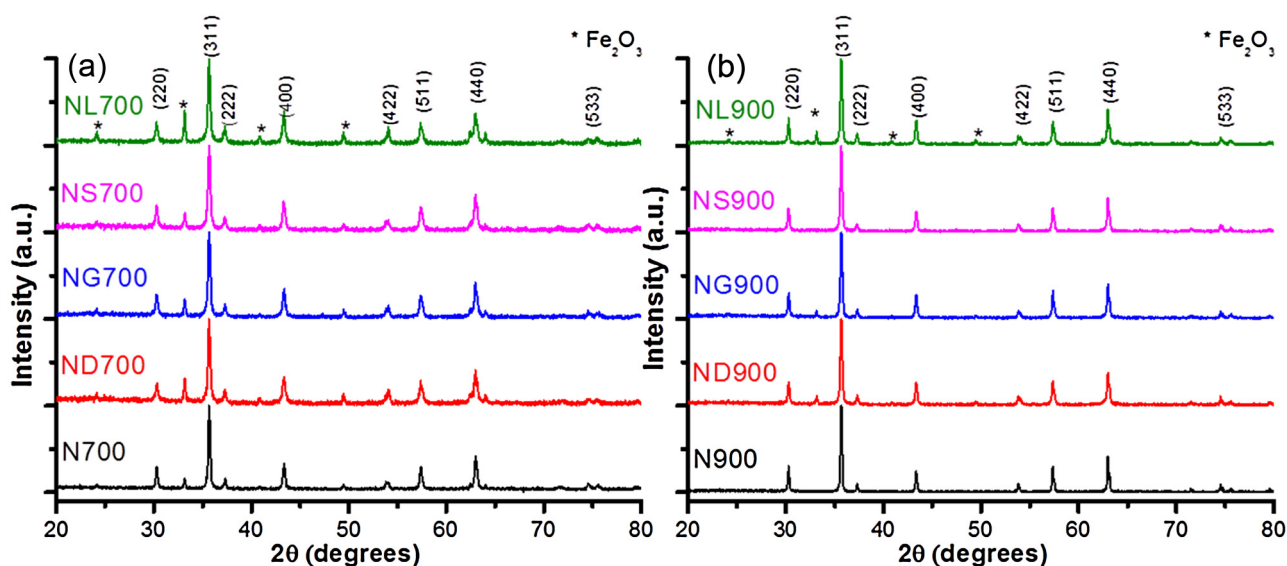
Fig. 1. XRD patterns of NiFe$_{1.98}$RE$_{0.02}$O$_4$ (RE = La, Sm, Gd and Dy) and NiFe$_2$O$_4$ samples annealed at (a) 700 °C and (b) 900 °C.

2.3. Catalytic activity evaluation

The degradation by CWPO processes of Orange II (Tropaeolin 000 No. 2) azo-dye with chemical formula C$_{16}$H$_{11}$N$_2$NaO$_4$S was investigated in this study.

For a typical run, 50 mL of 100 mg L^{-1} Orange II solution was heated up to the working temperature (75 °C). Consequently, the solution was acidified up to pH 2 and then 20 mM of hydrogen peroxide and 0.075 g of spinel ferrite catalyst in powder form were added under continuous stirring. This moment was taken as zero time in all degradation experiments. The volume of the reaction vessel was about 150 mL and the catalytic reactions were carried out, under complete darkness (to avoid any interference between the catalytic processes and the photocatalytic ones) in an orbital shaker (at 240 rotation/min) equipped with a temperature control system. The reaction was stopped at regular time intervals (2, 5, 9, 15 and 30 min), the catalyst was removed from the suspention by applying an external magnetic field and the analytical samples were extracted in order to evaluate the change in the concentration of each degraded solution by measuring the absorbance in range of 300–600 nm for Orange II with a SPECORD 200 Analytik Jena UV–vis spectrophotometer. The absorbance of Orange II solutions was determined at 485 nm and it was used to calculate the pollutant concentration. Note that, for every time interval a new catalytic test was conducted, in order to not affect the reaction result by stoping the processus for few seconds and to alter the color removal values by extracting, even a small amount, of pollutant.

Likewise, total organic carbon (TOC) concentration was analyzed with a AnalyticJena the multi N/C 2100 analyzer to evaluate the mineralization of the studied dye.

The degradation intermediate products of Orange II were identified by HPLC–MS using an Agilent 6500 Series Accurate-Mass Quadrupole Time-of-Flight (Q-TOF) LC/MS. Samples were separated on a Zorbax SB C18 (4.6 × 150 mm, 5 μm) reverse phase column. After the chromatographic detector, the system was fitted with a flow splitter, which directed 10% of the flow directly to the electrospray ion source (ESI) mass spectrometer. The ESI-Q/TOF MS conditions were set as follows: electrospray ionization (positive and negative ion mode), drying gas (N$_2$) flow rate 7.0 L/min; drying gas temperature 350 °C; nebulizer pressure 30 psig, capillary voltage 4000 V; fragmentation voltage 200 V; the full-scan mass spectra of the investigated compounds were acquired in the range

m/z 50–3000. Data were collected and processed using MassHunter Workstation Software Data Acquisition for 6200/6500 Series, version B.01.03.

3. Results and discussion

3.1. X-ray diffraction analysis

The X-ray diffraction patterns of the samples annealed at 700 °C for 5 h and at 900 °C for 7 h are shown in Fig. 1(a,b). The presence of (2 2 0), (3 1 1), (2 2 2), (4 0 0), (4 2 2), (5 1 1), (4 4 0) and (5 3 3) planes in all the recorded diffraction patterns confirms the formation of spinel ferrite for all the chemical compositions studied, according to JCPDS cards no. 44-1485 [29]. Nevertheless, for the materials heat-treated at 700 °C the pure spinel phase was not achieved (not even for the undoped nickel ferrite). This result is not very surprising. In a previous study related to the synthesis of nickel ferrite using various fuels like: cellulose, a cellulose–citric acid mixture, citric acid, tartaric acid, hexamethylenetetramine, glycine and urea we observed that only citric acid led to pure ferrite at 700 °C [30].

Note that, for all five samples, besides the characteristic diffraction peaks of spinel ferrite, some additional peaks appear, attributed to single iron oxide Fe$_2$O$_3$ (JCPDS No. 80-2377) [31]. Obviously, a corresponding amount of NiO should be observed. The lack of the peaks corresponding to NiO is explained by the fact that, according to the JCPDS No. 22-1189 [32], the peaks characteristics to this material usually appear at same values of 2θ as some peaks of spinel phase. Therefore, the NiO peaks are hidden in the majority phase XRD profile. Nevertheless, the presence of nickel oxide is clearly proved by the IR spectroscopy (see 3.2 Fourier transform-infrared spectroscopy analysis section). It is important to note that no diffraction lines attributed to rare-earth single oxide or rare-earth orthoferrite are observed. This fact suggests that maleic acid was very efficient to insert the bulky cation into the spinel matrix.

In order to achieve the pure spinel phase formation, the samples were supplementary heated for 7 h at 900 °C. The corresponding XRD patterns are depicted in Fig. 1b. Thus, we observed that for the undoped nickel ferrite (N900), and for the material doped with samarium (NS900) the diffraction lines attributed to the iron oxide were disappeared. This fact confirms the preparation of pure spinel phase. For the materials doped with lanthanum, gadolinium and dysprosium (NL900, NG900 and ND900) the impurity peaks are

Table 1
Experimental and calculated data obtained for $NiFe_{1.98}RE_{0.02}O_4$ (RE = La, Sm, Gd and Dy) and $NiFe_2O_4$ samples annealed at 900 °C.

Powder	XRD analysis			TEM analysis	Magnetic measurement	Size factor	Apparent kinetic constant
	a (Å)	d (Å)	D (nm)	$\bar{d}$ (nm)	Ms (emu/g)	$S_f = \frac{\bar{d}}{D}$	k (min^{-1})
NL900	8.34364	2.51570	34.4	55.9	21.9	1.625	0.1423
NS900	8.34526	2.51619	35.3	63.2	29.1	1.790	0.0735
NG900	8.34282	2.51545	36.5	59.5	27.4	1.630	0.1131
ND900	8.34480	2.51605	34.2	60.7	23.0	1.775	0.0820
N900	8.34538	2.51623	48.0	108.7	33.0	2.265	0.0295

Table 2
The IR absorption bands of $NiFe_{1.98}RE_{0.02}O_4$ (RE = La, Sm, Gd and Dy) and $NiFe_2O_4$ samples annealed at 700 °C and 900 °C.

Powder	v_1 (cm^{-1})	v_2 (cm^{-1})	v_3 (cm^{-1})	Powder	v_1 (cm^{-1})	v_2 (cm^{-1})	v_3 (cm^{-1})
NL700	586.0	409.7	469.3	NL900	586.9	402.8	478.8
NS700	585.0	400.8	469.6	NS900	587.1	400.9	–
NG700	586.9	402.3	471.1	NG900	592.1	401.5	470.0
ND700	585.9	405.6	471.4	ND900	594.7	403.6	467.7
N700	583.9	410.1	475.1	N900	596.7	406.3	–

still present, even if their intensity is much smaller reported to the samples sintered at 700 °C, indicating a decrease in single oxides amount.

As observed from XRD patterns the insertion of the rare-earth cations into the spinel matrix was successfully achieved by using maleic acid as fuel even if it is expected to be difficult, because of their higher ionic radius (1.032 Å for La^{3+}, 0.958 Å for Sm^{3+}, 0.938 Å for Gd^{3+} and 0.912 Å for Dy^{3+}, respectively) as compared to Fe^{3+} (0.645 Å) [24,33].

The main crystallographic data obtained from XRD patterns recorded for the materials sintered at 900 °C are given in Table 1. Thus, Table 1 summarizes the values for lattice parameter (a), interplanar distance (d) and mean crystallite size (D), calculated using Laue, Bragg, and Debye–Scherrer equations, respectively, as presented in previous works [24,30]. Note that, the five most intense peaks were used for crystallite size calculation.

The doping with RE cations generates a slight decrease of lattice parameter and interplanar distance values from 8.34538 to 8.34364 Å and from 2.51623 to 2.51570 Å, respectively, for all the investigated lanthanides. This behavior is explained in the literature by the larger radius of doping cations, leading to the lattice distortion and to lower degrees of alignment of spinel lattice fringes [24,34]. Moreover, the decrease of (a) parameter is often explained by a rearrangement of the cations between the tetrahedral and octahedral sites in order to achieve the lattice strain relaxation [35]. Nickel ferrite is a totally inverted spinel with the totality of nickel cations distributed in the octahedral sites and iron cations equally distributed in the octahedral and tetrahedral sites [36]. Normally, while doping spinel ferrites, the dopant may replace atoms in both sites, if the ionic radii are adequate. Nevertheless, in the particular case of rare-earth doped ferrite, because of the higher ionic radii it is expected that the dopant cations to be distributed in the octahedral sites, which are larger compared to the tetrahedral ones. This fact generate a partial migration of nickel cations from octahedral to tetrahedral sites accompanied by the migration of equivalent number of iron cations from tetrahedral to octahedral lattices. Therefore, the octahedral strain relaxation takes place, because of the smaller ionic radii of Fe^{3+} (0.645 Å) compared to Ni^{2+} (0.69 Å) [35]. However, no strict correlation between rare-earth cation radius and the decrease of (a) and (d) parameters could be established. Moreover, it could be noticed that the values obtained for samarium doped sample are very close to the undoped material. Therefore, the variation of lattice parameter and interplanar distances depends on the phase purity.

Likewise, we observed a dramatic decrease of the mean crystallite size, from 48 nm for the nickel ferrite sample to about 35 nm

for the doped compounds. These results are in good agreement with the literature and confirm that the growth of the crystallites is strongly affected by the replacement of a small amount of Fe^{3+} with rare earth cations, leading to smaller values [15,24].

3.2. Fourier transform-infrared spectroscopy analysis

The IR spectra recorded in the 900–350 cm^{-1} region at room temperature of the materials sintered at 700 °C and at 900 °C are shown in Fig. 2(a,b) and the band position of all the studied materials are listed in Table 2. Commonly, the infrared spectra of spinel ferrites consist of two strong absorption bands in the range 400–600 cm^{-1}: v_1 (~600 cm^{-1}) attributed to the stretching vibration of the tetrahedral metal–oxygen bond and v_2 (~400 cm^{-1}) attributed to the octahedral metal–oxygen bond, respectively [24]. For our samples, these bands are clearly observed whatever the sintering temperature was. However, careful inspection of IR spectra revealed the presence of a third band (v_3) at ~470 cm^{-1} for all the samples presenting impurities in XRD patterns (all the materials heat treated at 700 °C and the materials doped with La, Gd and Dy annealed at 900 °C). This band can be attributed either iron oxide or nickel oxide. The existing data in literature indicate that each of the Fe_2O_3 and NiO oxide presents two bands in the infrared spectra at ~530 and ~450 cm^{-1} as well as at ~620 and ~470 cm^{-1}, respectively [32,37]. In the spectra registered for our materials, the iron oxide bands and the band of nickel oxide at the higher wave number are superimposed with those assigned to the spinel ferrite. Therefore, in our particular case, the third band (v_3) is attributed to the vibration of Ni—O bond [32]. Hence, the IR spectroscopy data strongly correlate with the XRD commentaries. By using maleic acid as the fuel agent, only two pure-phase spinel compounds were obtained, i.e. N900 and NS900.

For the materials sintered at 900 °C, the slight shifts to lower wave numbers observed for both v_1 and v_2 bands is explained by the perturbation occurring in the Fe–O bond, and by iron and nickel cations migration between the tetrahedral and octahedral sites, caused by the replacement of a small amount of Fe^{3+} with RE^{3+}. This fact clearly proves the successful insertion of rare-earth cations into the spinel matrix.

3.3. Transmission electron microscopy and EDS analysis

Fig. 3(a–f) illustrates some representative examples of TEM and HRTEM photomicrographs, as well as the corresponding curves of the probability density function for particle size distribution of the
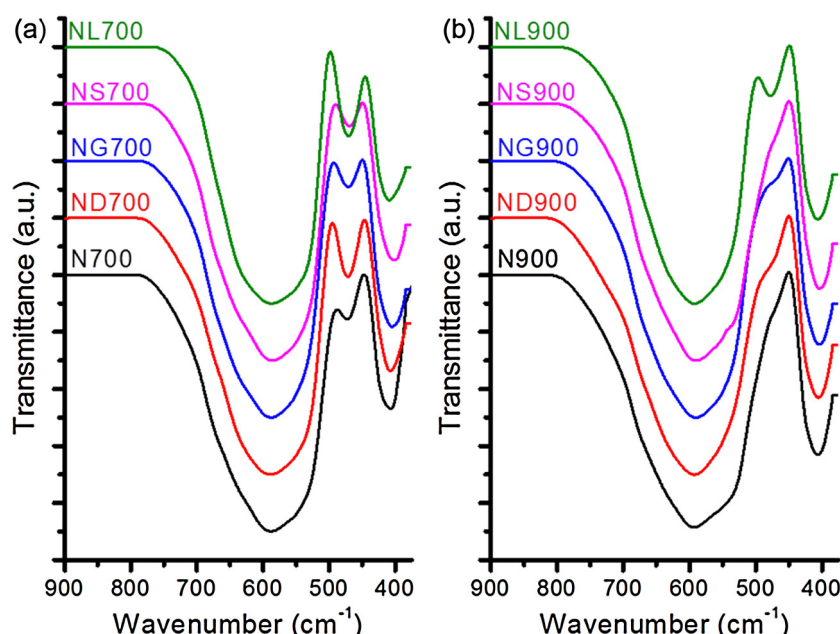
Fig. 2. IR spectra of NiFe$_{1.98}$RE$_{0.02}$O$_4$ (RE = La, Sm, Gd and Dy) and NiFe$_2$O$_4$ samples annealed at (a) 700 °C and (b) 900 °C.

samples sintered at 900 °C. The average particle sizes ($\bar{d}$) calculated from TEM micrographs are reported in Table 1. The formation of nanometric particles with irregular shapes is highlighted on TEM pictures, for all produced materials. The average grain size data from Table 1 and the particle size distribution from Fig. 3f show a significant influence of the doping with rare-earth cations over the grain size and grain size distribution of nickel ferrite. Thus, the average particle sizes strongly decrease to 55.9–63.2 nm for the materials containing RE ions, compared to 108.7 nm for the N900 sample. Likewise, it could be noticed that the distribution of particle sizes for the undoped sample (N900) is very broad, ranging from 20 to 200 nm, and it shifts to the left and becomes narrower for the doped materials, ranging from 20 to 105 nm. The high resolution images confirm the nanometric sizes and irregular shapes of the studied catalysts particles. Moreover, the crystalline structure of the materials, observed from XRD patterns, is confirmed by the fringe pattern. As an example, the fringe pattern observed for a NL900 nanoparticle (Fig. 4a insert) is typical for the spinel ferrite system and clearly proves that the particle is single crystalline with no defect, according to the related literature [38].

Fig. 4(a–f) depicts EDS spectra of the studied samples sintered at 900 °C. The bands of Ni, Fe, O and RE, respectively, are clearly observed in these spectra. The presence of the rare-earth cations is undoubtedly confirmed, in spite of their low concentrations in the samples. Moreover, no impurity lines were detected, proving the high purity of the materials.

3.4. Magnetic properties

One of the main advantages of using spinel ferrite catalysts in CWPO processes is the possibility of easily recover them from the reaction environment after usage because of their magnetic properties. In this respect, the magnetic behavior of the samples sintered at 900 °C was studied. The hysteresis loops registered at room temperature are depicted in Fig. 5, and the values for saturation magnetization (M_s) are listed in Table 1. First, the ferrimagnetic behavior and the magnetization value (33 emu/g) observed for nickel ferrite (N900) synthesized using maleic acid as fuel were found to be in close agreement with literature data [39]. Second, concerning the magnetic performances of doped ferrites, one

can notice that the replacement of a small amount of Fe^{3+} ions by RE^{3+} ions reduces the net magnetic moment, and this caused a slightly decrease of magnetization values. These results are in agreement with our previous findings [15,24], where we demonstrated that the doping of spinel ferrites with different lanthanide cation slightly alter the magnetic performance, whatever the combustion agent was used during synthesis. This fact is explained by the weak magnetic exchange interaction betwen RE^{3+} and Fe^{3+} (4f-3d electron coupling) induced by the replacement of ferric ions [15].

Nevertheless, in spite of M_s decrease with doping the nickel ferrite with small amount of rare-earth cations, the observed values still remain suitable for extracting the solid catalyst from the aqueous environment by applying an external magnetic field.

3.5. Catalytic properties

3.5.1. Catalytic activity of NiFe$_{1.98}$RE$_{0.02}$O$_4$ (RE = La, Sm, Gd and Dy) and NiFe$_2$O$_4$ catalysts sintered at 900 °C for CWPO of Orange II

The efficiency of NiFe$_{1.98}$RE$_{0.02}$O$_4$ (RE = La, Sm, Gd and Dy) and NiFe$_2$O$_4$ samples sintered at 900 °C as catalysts in CWPO processes of Orange II was evaluated at 75 °C.

Fig. 6(a–e) shows the change of UV–vis spectra of Orange II during catalytic wet hydrogen peroxide oxidation in the presence of the catalysts (sintered at 900 °C) at different time intervals (0, 2, 5, 9, 15, and 30 min). In the range of 300–600 nm, Orange II UV–vis spectra present three absorption peaks: at 310 nm (ascribed to naphthalene ring), at 400 nm (attributed to n-π* transitions of azo group) and the maximum absorption peak located at 485 nm (originated from the N=N bond) [40,41]. One can observe from Fig. 6 that all peaks of Orange II became weaker along with the reaction time, which indicated that azo group and the naphthalene part of the Orange II molecule were attacked by the presence of all studied catalysts. It was observed that the color removal of 100 mg L^{-1} Orange II was practically complete for the NL900 and NG900 catalysts, while for the N900 sample, after 30 min of reaction, the color was still present. Thus, in order to adequately compare the performances of the studied materials, the evolutions of Orange II concentrations during the CWPO processes as a function of time and the dye removal efficiency observed after 15 min of reaction,
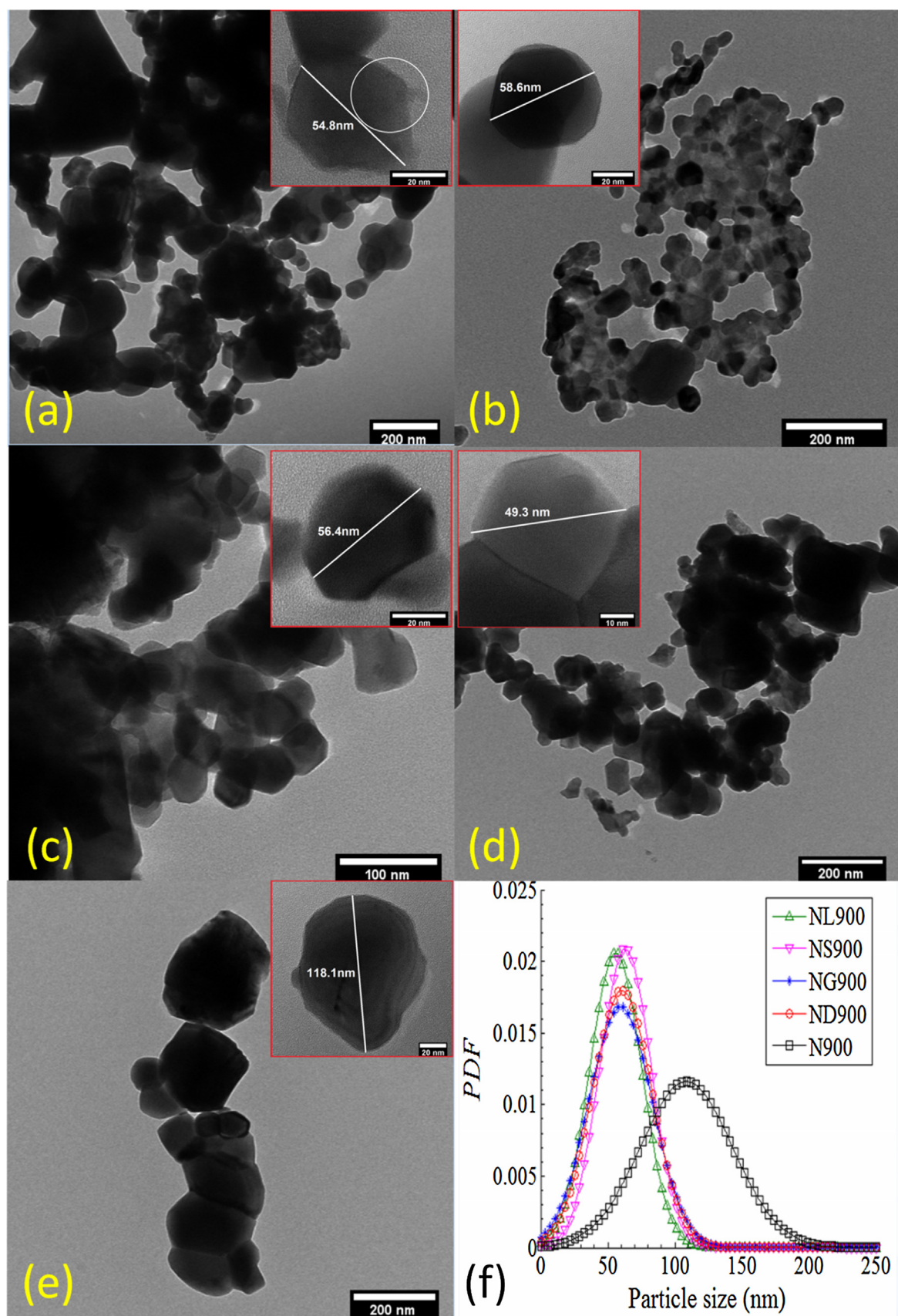
Fig. 3. Representative TEM and HRTEM (insert) photomicrographs of samples: (a)NiFe$_{1.98}$La$_{0.02}$O$_4$(NL900), (b)NiFe$_{1.98}$Sm$_{0.02}$O$_4$(NS900), (c)NiFe$_{1.98}$Gd$_{0.02}$O$_4$(NG900), (d)NiFe$_{1.98}$Dy$_{0.02}$O$_4$(ND900), (e)NiFe$_2$O$_4$(N900) annealed at 900 °C and (f) Probability density functions (normal distribution) of particle size.
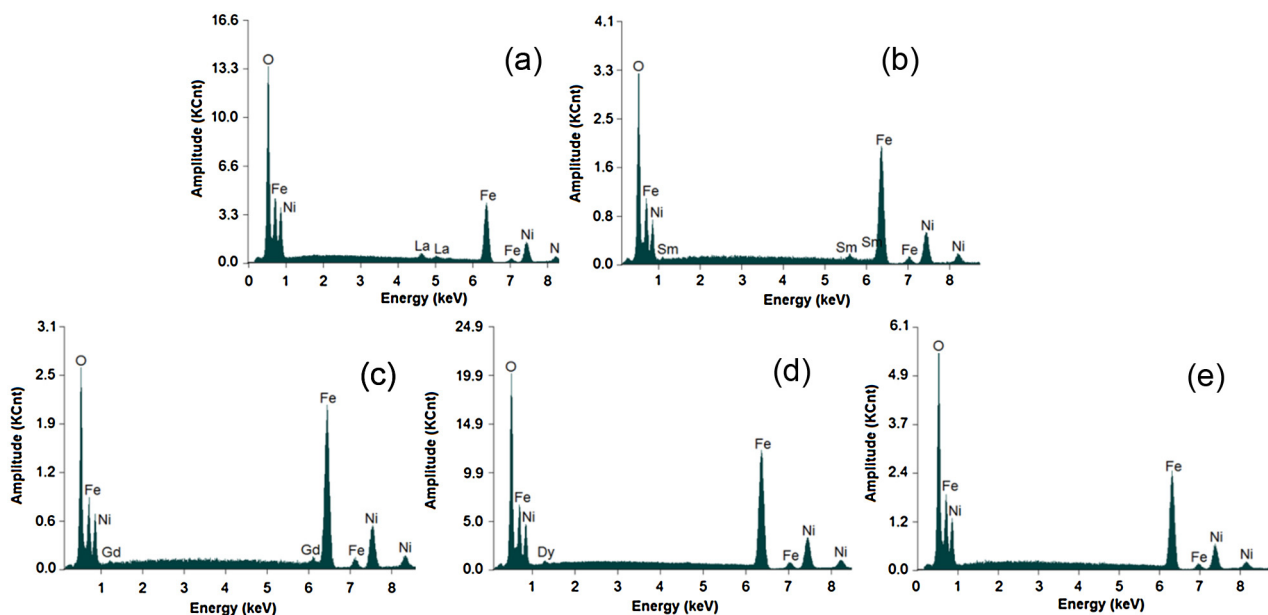
Fig. 4. EDS spectra of samples: (a)NiFe$_{1.98}$La$_{0.02}$O$_4$(NL900), (b)NiFe$_{1.98}$Sm$_{0.02}$O$_4$(NS900), (c)NiFe$_{1.98}$Gd$_{0.02}$O$_4$(NG900), (d)NiFe$_{1.98}$Dy$_{0.02}$O$_4$(ND900), (e)NiFe$_2$O$_4$(N900) annealed at 900 °C.
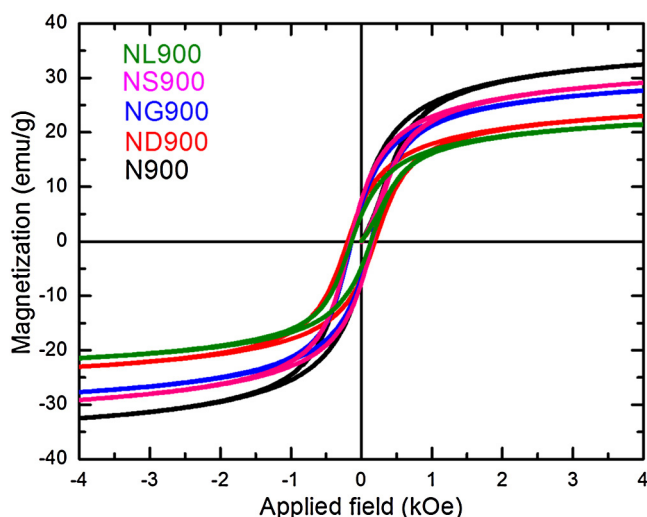
Fig. 5. Room temperature hysteresis loops for NiFe$_{1.98}$La$_{0.02}$O$_4$(NL900), NiFe$_{1.98}$Sm$_{0.02}$O$_4$(NS900), NiFe$_{1.98}$Gd$_{0.02}$O$_4$(NG900), NiFe$_{1.98}$Dy$_{0.02}$O$_4$(ND900), NiFe$_2$O$_4$(N900) samples annealed at 900 °C.

in the presence of studied ferrite catalysts, are plotted in Fig. 7(a,b). First of all, it must be noticed that all the materials doped with rare earth ions are much more catalytically active than the undoped nickel ferrite catalyst, all over the reaction time interval considered. Moreover, after 15 min of the catalytic process, the color removal efficiency was ranging from 69.6 to 90.6% for the catalysts doped with lanthanide cations, compared to only 30.6% calculated for nickel ferrite. Among the catalysts containing rare-earth, the best catalytic performance was attributed to the NL900 sample, followed in order by NG900, ND900, and finally by NS900. For comparison, Binxia et al. [42] reported 97.9% decolorization of Orange II after 60 min of reaction (at 60 °C and pH = 3) using montmorillonite pillared with Fe-Ni-Al as catalysts. Note that, for the NL900 sample, the total organic carbon removal after 30 min of reaction was 61.7%. In order to understand the degradation pathway of Orange II, the identification of intermediates products was performed using HPLC–MS analysis. Fig. 8(a,b) depicts the HPLC chromatograms of

initial Orange II, and after 30 min of reaction in the presence of the NL900 catalyst. First, for the initial solution it was observed a single peak at R$_t$ = 10.535 min attributed to Orange II, as confirmed by the MS analysis (m/z ratio of 327) (see Fig. 8a insert). Second, in the chromatogram collected for the solution recovered after the catalytic test this peak disappeared, which confirmed the complete degradation of the studied dye by the NL900 catalyst, in good agreement with the UV–vis data. The MS analysis carried out for the second solution revealed the presence of three intermediates at m/z ratio of 172, 165 and 103. According to the literature, the ion with m/z ratio of 172 indicated the presence of the sulphanilic acid [43]. Likewise, the ions with m/z ratio of 165 and 103 proved the presence of phthalic and malonic acids, respectively, derived from the naphthalene structure of the Orange II dye. These data suggested that the Orange II degradation mechanism involved, in a first step, the N=N bond cleavage. Consequently, the as-obtained aromatic intermediates were transformed, by ring-opening processes, into short-chain aliphatic acids. Finally, these organic acids were mineralized into innocuous inorganic compounds (CO$_2$ and H$_2$O).

According to the literature the catalytic activity of the spinel ferrites depend on both their physical and chemical properties [12]. Previously, we demonstrated that the catalytic performance of spinel ferrite catalysts, in degradation processes in aqueous environment, is often correlated with the crystallite size (D) [44] or the particle size ($\bar{d}$) [15] of materials. However, in the present work, we were not able to find a direct correlation between the catalytic behavior and one of these two parameters considered separately. But, if we consider the ratio particle size to crystallite size, named in this paper as the size factor (S_f), we observe a very good agreement between this factor and the catalytic performances (see Table 1). Hence, the smaller size factor is, the greater color removal efficiency is. In conclusion, the observed improvement of the catalytic properties of doped ferrites is owing to the combined effect of reduction of both particle and crystallite sizes.

On the other hand, literature reports showed that the catalytic performances of spinels depend on the cation distribution among the octahedral and tetrahedral lattices. It was demonstrated that, the octahedral sites are mainly oriented at the surface of spinel ferrite powders and, therefore, catalytic activity of this kind of
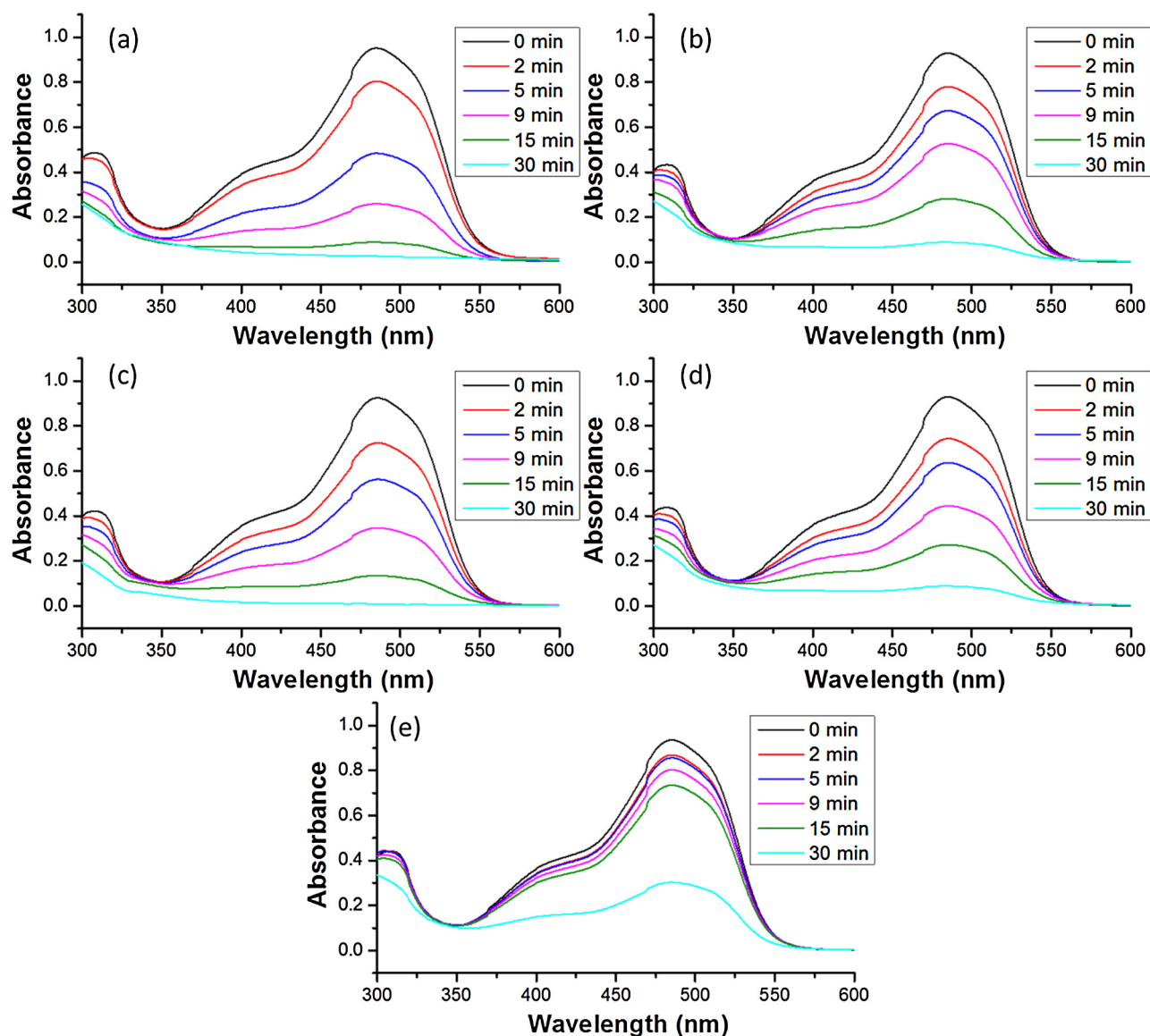
Fig. 6. Spectral response of 100 mg L^{-1} Orange II during the catalytic degradation in the presence of samples (a)NiFe$_{1.98}$La$_{0.02}$O$_4$(NL900), (b)NiFe$_{1.98}$Sm$_{0.02}$O$_4$(NS900), (c)NiFe$_{1.98}$Gd$_{0.02}$O$_4$(NG900), (d)NiFe$_{1.98}$Dy$_{0.02}$O$_4$(ND900), (e)NiFe$_2$O$_4$(N900) annealed at 900 °C.

materials is correlated to the octahedral cations nature [12]. In our particular case, the XRD and FT-IR analysis, proved the insertion of the rare-earth cations into the spinel matrix. The decrease of the lattice parameter, correlated with shifts observed for v_1 and v_2 infra-red bands, indicates that during the insertion of the lanthanide bulky cations in the spinel structure a part of iron cations migrated from tetrahedral to octahedral sites. Therefore, after doping, the surface of the nickel ferrite powder is richer in catalytically active iron cations.

3.5.2. Kinetics of CWPO of Orange II

Normally, the degradation of the dye by CWPO processes should be described as a second-order reaction. However, assuming that hydroxyl radical (HO•) instantaneous concentration is constant, because of the large excess concentration of H$_2$O$_2$, the kinetics of Orange II removal could act according to the pseudo-first-order model [41] (see Eq. (1)):

$$C = C_0 e^{-kt} \tag{1}$$

where C and C_0 are the concentration of Orange II at time t and initial concentration, respectively; and k is the reaction rate constant. In order to validate the applicability of the pseudo-first-order kinetic model, collected data were fitted to the above mentioned equation (Eq. (1)) by nonlinear regression (see Fig. 7a). In this respect, the Gauss-Newton method was employed, and computations were done using *nlinfit* solver implemented in the matlab program. The nonlinear regression technique enabled to determine the apparent reaction rate constants (k).

The calculated values for rate constants (k), listed in Table 1, are in reasonable agreement with the size factor. As the size factor decreases, the reaction rate constant increases. The fastest Orange II azo dye degradation was observed for the NL900 sample, with a reaction rate constant of 0.1423 min^{-1}. In turn, the N900 sample removed the same amount of dye about 5-fold slower, with a rate constant of 0.0295 min^{-1}. Other catalysts presented intermediate values and confirmed the good correlation between the size factor and the reaction rate constant.
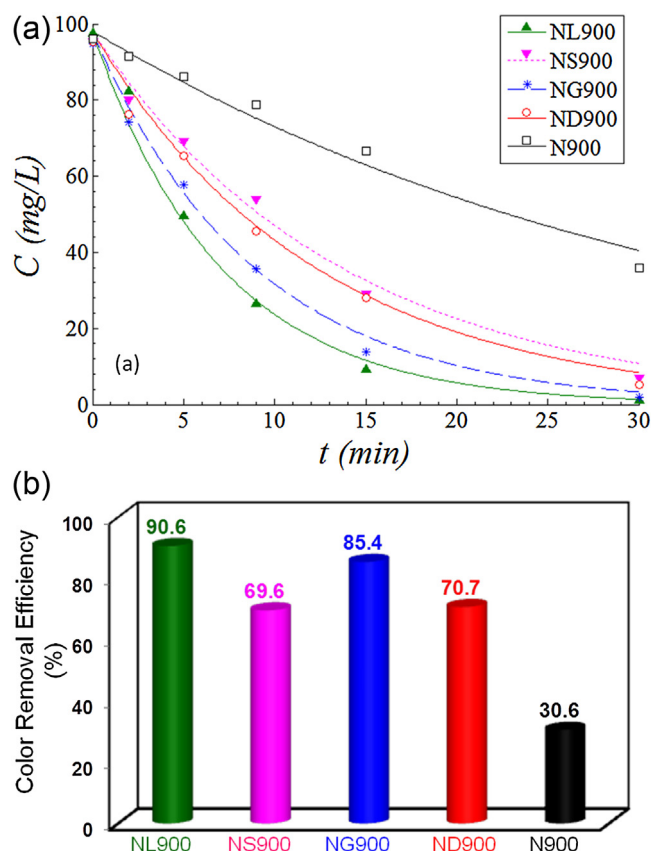
Fig. 7. (a) Catalytic degradation of $100 \, \text{mg} \, \text{L}^{-1}$ Orange II as a function of time (fitted lines by pseudo first-order-kinetic model); and (b) Color removal efficiency at 15 min of catalytic reaction, in the presence of samples: $NiFe_{1.98}La_{0.02}O_4$(NL900), $NiFe_{1.98}Sm_{0.02}O_4$(NS900), $NiFe_{1.98}Gd_{0.02}O_4$(NG900), $NiFe_{1.98}Dy_{0.02}O_4$(ND900), $NiFe_2O_4$(N900) annealed at 900 °C.

3.6. Desirability function approach (DFA)

In order to select the optimal material for dye degradation application, the desirability function approach (DFA) was employed. This method (DFA) is widely used to address a multi-objective optimization problem, i.e. the optimum should be decided based on several criteria (standpoints). In our case, the optimization criteria were: high catalytic performance, proper morphology and good magnetic properties of the produced material. Accordingly, four responses were considered along with this line, namely: (a) color removal efficiency; (b) rate constant of catalytic reaction; (c) factor size and (d) magnetic saturation of the catalyst. All these responses were taken into account by desirability function approach to decide the best (optimal) material for heterogeneous catalytic application. Hence, the optimal catalyst should satisfy all considered criteria combined into a maximum synergetic effect. Note that, we included the magnetic property in DFA methodology in order to consider the abilities

of catalysts to be easily removed from the reaction environment under the external magnetic field after usage.

The desirability function approach involves the calculation of individual desirability functions (δ_i) by converting the actual values of responses into the scaled (normalized) ones ranging from 0 to 1. Actual values of responses are listed in Table 1 for the magnetic saturation, size factor and apparent kinetic constant, respectively. And, the real values of color removal efficiency are given in Fig. 7(b).

The individual desirability functions for the responses that should be maximized (i.e. color removal efficiency, rate constant and magnetic saturation) were calculated using the conversion scheme of type LTB (the-larger-the-best) that can be written as follows [45,46]:

$$LTB : \delta_j = \begin{cases} 0, & \text{if} y_j \leq y_j^{LB} \\ \left(\dfrac{y_j - y_j^{LB}}{y_j^{UB} - y_j^{LB}} \right), & \text{if} y_j^{LB} \leq y_j \leq y_j^{UB} \\ 1, & \text{if} y_j \geq y_j^{UB} \end{cases} \quad (2)$$

where y_j is the actual value of the response with index j; y_j^{LB} is the lower-bound limit and y_j^{UB} is the upper-bound limit of the response; δ_j denotes the individual desirability (i.e. normalized value) of the response. In turn, the individual desirability function for the size factor (i.e. response to be minimized) was computed using the conversion of type STB (the-smaller-the-best) that is given by the following expression [45,46]:

$$STB : \delta_j = \begin{cases} 1, & \text{if} y_j \leq y_j^{LB} \\ \left(\dfrac{y_j - y_j^{UB}}{y_j^{LB} - y_j^{UB}} \right), & \text{if} y_j^{LB} \leq y_j \leq y_j^{UB} \\ 0, & \text{if} y_j \geq y_j^{UB} \end{cases} \quad (3)$$

For further calculation of the global desirability, each individual desirability function should be powered by an *importance factor* (*I*) or *weight factor* attributed to each response. Values of *importance* were equal to 1 (for less important responses) and 2 (for more important responses). In our case, responses with less importance ($I_1 = 1$ and $I_2 = 1$) for catalytic reaction were: the magnetic saturation and size factor, respectively. In turn, responses with more importance ($I_3 = 2$ and $I_4 = 2$) for catalytic application were: the apparent kinetic constant and color removal efficiency, respectively. Finally, the individual desirability functions (δ_i) were aggregated into a composite function, known as the global desirability (D_G), which was calculated as the geometric mean according to the following equation [45,46]:

$$D_G = \left(\prod_{j=1}^{n} \delta_j^{I_j} \right)^{\frac{1}{\sum I_j}} \quad (4)$$

Table 3
Results of optimization by desirability function approach (DFA): individual desirability and global desirability values.

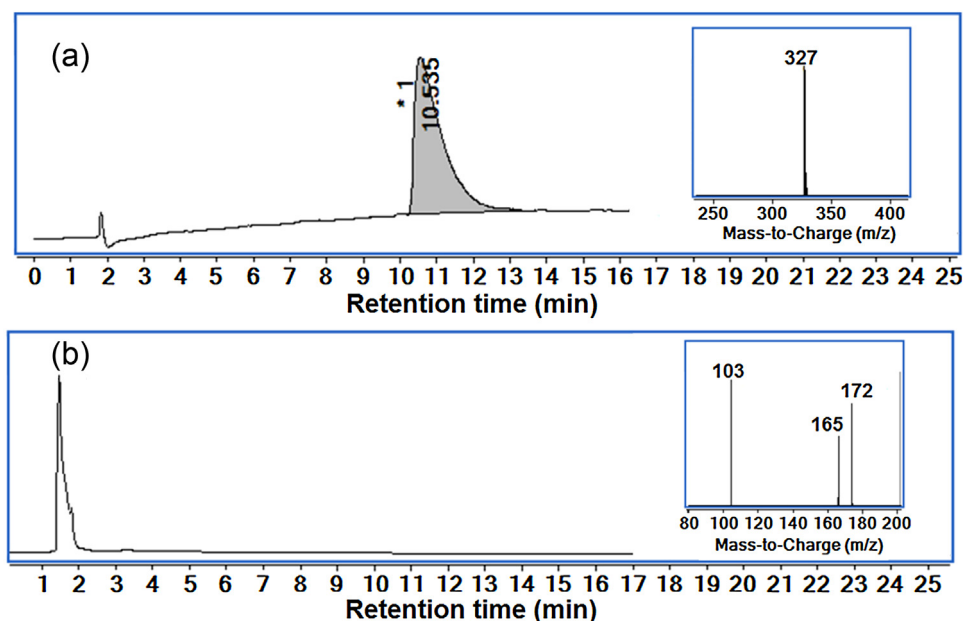| Catalyst Sample (Powder)	Individual desirability for saturation magnetization δ_1 ($I_1 = 1$)	Individual desirability for size factor δ_2 ($I_2 = 1$)	Individual desirability for apparent kinetic constant δ_3 ($I_3 = 2$)	Individual desirability for color removal efficiency δ_4 ($I_4 = 2$)	Global Desirability D_G
NL900	0.476	0.917	0.945	0.937	0.836
NS900	0.764	0.807	0.454	0.637	0.610
NG900	0.696	0.913	0.736	0.863	0.797
ND900	0.520	0.817	0.514	0.653	0.603
N900	0.920	0.490	0.138	0.077	0.193

Fig. 8. HPLC chromatograms and MS spectra (insert) of (a) initial Orange II and (b) after 30 min of catalytic reaction, in the presence of the NiFe$_{1.98}$La$_{0.02}$O$_4$(NL900) sample.

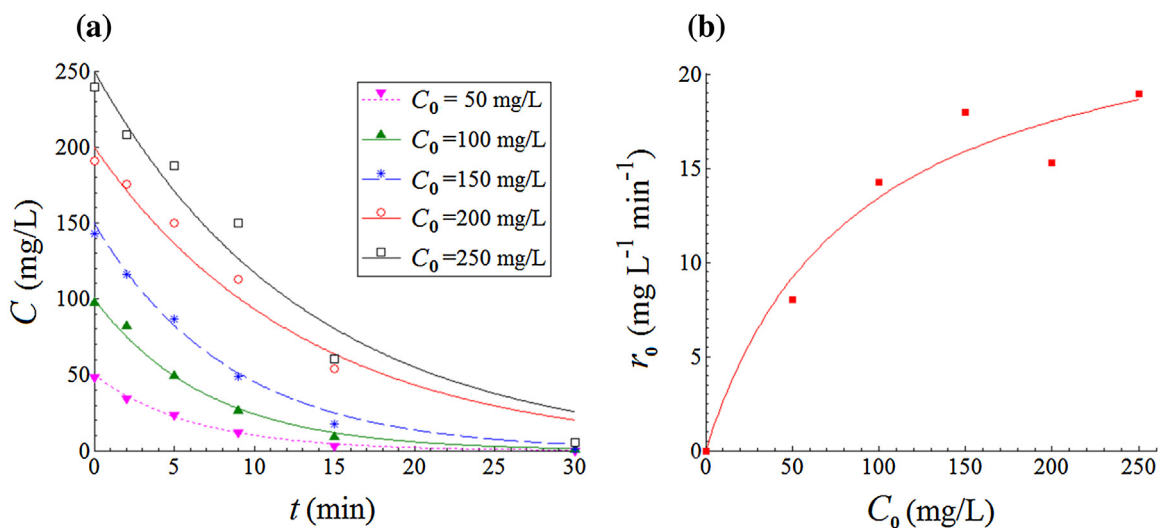**Fig. 9.** (a) Catalytic degradation of 50, 100, 150, 200 and 250 mg L^{-1} Orange II as a function of time (fitted lines by pseudo-first-order kinetic model); and (b) Kinetic plots r_0 vs. C_0 for Orange II CWPO, in the presence of NiFe$_{1.98}$La$_{0.02}$O$_4$(NL900) annealed at 900 °C (fitted solid line by Langmuir-Hinshewood model).

For our peculiar case with four responses ($n = 4$) considered at different importance (i.e. $I_1 = 1$; $I_2 = 1$; $I_3 = 2$ and $I_4 = 2$), Eq. (4) can be re-written as follows:

$$D_G = \sqrt[6]{\delta_1 \times \delta_2 \times \delta_3^2 \times \delta_4^2} \tag{5}$$

According to the DFA methodology, optimal conditions are determined by the highest value of the overall desirability ($D_G \rightarrow 1$). Results of desirability function approach are summarized in Table 3. As can be seen from Table 3, the optimal material for catalytic application is NL900 (i.e. NiFe$_{1.98}$La$_{0.02}$O$_4$ sintered at 900 °C), which yielded the highest value of the global desirability ($D_G = 0.836$). The tested catalysts can be arranged in the order of global desirability decreasing as follows: NL900 > NG900 > NS900 > ND900 > N900. Thus, it can be inferred that the doped materials with rare-earth cations are superior to pure nickel spinel ferrite (N900) in terms of global desirability. Therefore, the doped products are more appropriate for catalytic degradation of dyes from wastewaters.

3.7. Langmuir–Hinshelwood model applied for CWPO of Orange II in the presence of NiFe$_{1.98}$La$_{0.02}$O$_4$ sintered at 900 °C

The Langmuir-Hinshelwood equation is the most appropriate model used to describe the kinetics of heterogeneous catalytic reactions [47]. The Langmuir-Hinshewood expression has been developed to determine the relationship between the initial degradation rate and the concentration of the organic pollutant. It has been successfully applied for the case of reactions occurring at the solid-liquid interface within heterogeneous catalytic processes (e.g. photocatalysis, CWPO), and it is given by the following equation [47,48]:

$$r_0 = \frac{dC}{dt} = \frac{k_r K_L C_0}{1 + K_L C_0} \tag{6}$$

where r_0 denotes the initial rate of disappearance of the organic pollutant (Orange II), C_0 – initial Orange II concentration, K_L – equilibrium constant for adsorption of Orange II molecules onto
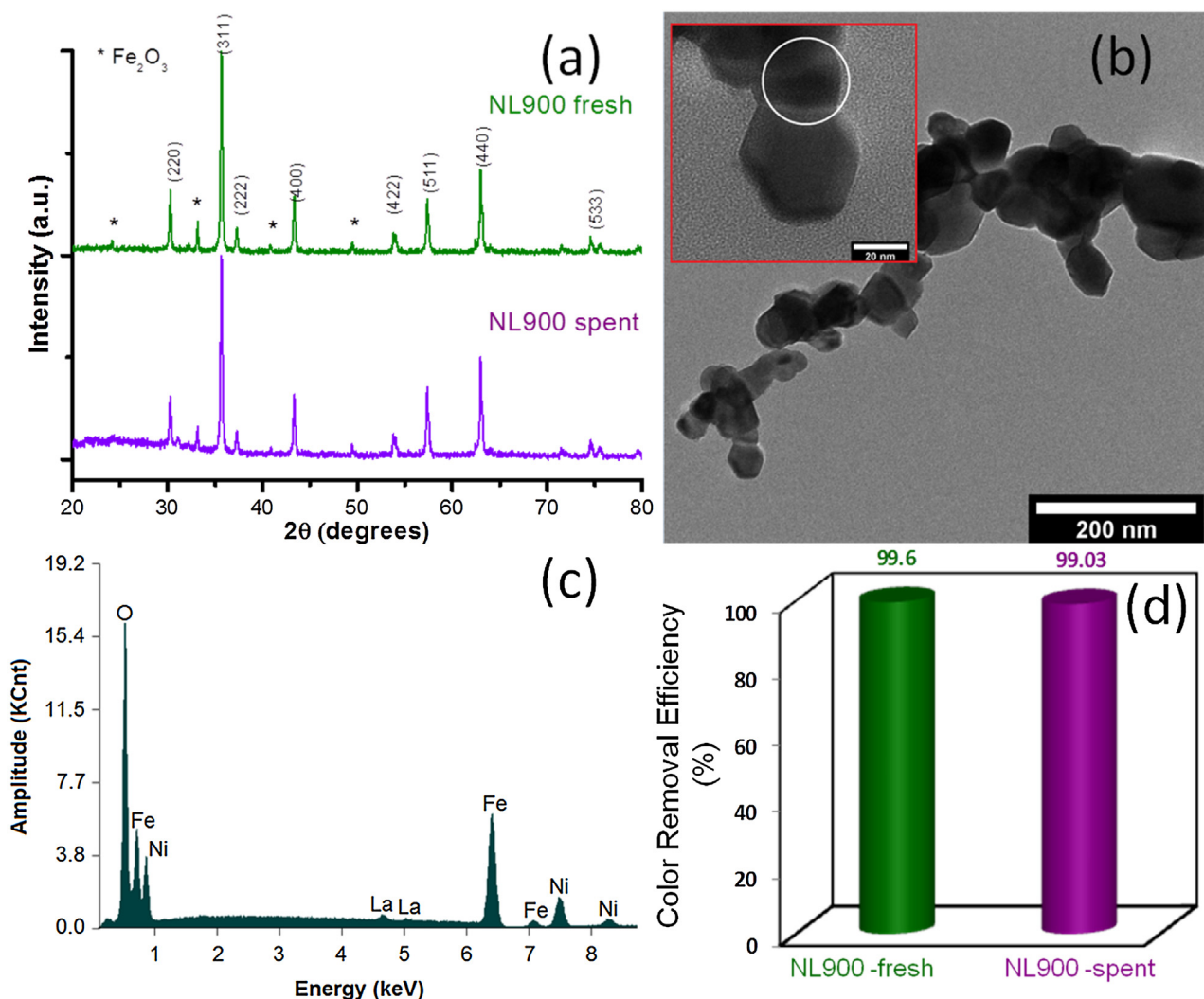
Fig. 10. (a) XRD patterns of NiFe$_{1.98}$La$_{0.02}$O$_4$ (NL900) fresh and spent catalysts; (b) Representative TEM and HRTEM (insert) photomicrographs of NiFe$_{1.98}$La$_{0.02}$O$_4$ (NL900) spent catalyst; (c) EDS spectra of NiFe$_{1.98}$La$_{0.02}$O$_4$ (NL900) spent catalyst; (d) color removal at 30 min of catalytic reaction, in the presence of: NiFe$_{1.98}$La$_{0.02}$O$_4$ (NL900) fresh and spent catalysts.

the catalyst surface and k_r is the reaction rate constant accounting for the tendency of the organic compound to be decayed after adsorption. Hence, the Langmuir-Hinshewood model describes two phenomena occurring in a heterogeneous catalytic process: (1) adsorption of the organic substrate onto solid surface of the catalyst; and (2) kinetics of chemical reaction for the decay of the organic pollutant.

In this work, we have investigated the catalytic behavior of the optimal material NL900 (NiFe$_{1.98}$La$_{0.02}$O$_4$) for the degradation of Orange II dye at different initial concentrations. Fig. 9a shows the evolutions of Orange II azo-dye concentrations during the CWPO reactions as a function of time, in the range of 50–250 mg L^{-1} initial pollutant concentration. It must be noticed that the NL900 material proved remarkable catalytic performances for all the selected initial pollutant concentration. For each starting concentration considered, the Orange II color removal was practically complete after 30 min of reaction in the presence of the optimal catalyst (NL900). We observed that the apparent kinetic constant, calculated by Eq. (1), decreased (from 0.1601 to 0.0757 min^{-1}) with the increment of the initial dye concentration (see Table 4). This might be explained by the fact that the effective degradation of the dye molecules from a more concentrated solution requires a greater time than from the diluted solutions.

Table 4
Kinetic parameters for Orange-II degradation by NL900 catalyst at various initial dye concentration.

Initial dye concentration, C_0 (mg/L)	Apparent kinetic constant, k (min^{-1})	Initial reaction rate, r_0 (mg L^{-1} min^{-1})
50	0.1601	8.005
100	0.1423	14.230
150	0.1197	17.955
200	0.0764	15.280
250	0.0757	18.925

The calculated initial rate values (r_0) are summarized in Table 4; and the r_0 vs. C_0 plot is depicted in Fig. 9b. One may observe that the initial reaction rate strongly depends on the initial Orange II concentration. And, it increases from $r_0 = 8.005$ (mg L^{-1} min^{-1}) at the lowest dye concentration to $r_0 = 18.925$ (mg L^{-1} min^{-1}) at the highest pollutant concentration.

Values of model parameters k_r and K_L were calculated according to Eq. (6) by nonlinear regression using Gauss-Newton method and *nlinfit* matlab solver. In our case, Langmuir-Hinshewood parameters were equal to $k_r = 25.0508$ (mg L^{-1} min^{-1}) and $K_L = 0.0116$ (mg^{-1} L). Because $k_f \gg K_L$, it may be inferred that the fast color

removal in the presence of NL900 sample was mainly attributed to the chemical decay reaction. In turn, the adsorption of the dye molecule onto the catalyst surface was of minor significance. These results are in close agreement with literature data. For instance, Liang et al. observed that the decolorization rate just by adsorption was below 5% when they studied the Orange II catalytic decay by magnetite-based catalysts [41].

3.8. Stability of $NiFe_{1.98}La_{0.02}O_4$ sintered at $900\,^{\circ}C$ catalyst

In order to study the stability of the most promising catalyst, the NL900 material was recovered after the catalytic test, washed three times with ethanol and dried in oven for several hours. The material was characterized by XRD, TEM and EDS before a re-use test, carried out in similar conditions as for the fresh catalysts. The obtained results are shown in Fig. 10(a–d). First, it was observed a perfect match between the X-ray diffraction patterns of the fresh and spent samples (Fig. 10a). This proved that, during the catalytic process, the catalyst maintained his crystalline structure. Moreover, the results obtained for TEM, HRTEM and EDS (Fig. 10b,c) analysis were not different than those obtained for the fresh catalyst and confirmed the stability of the material in the catalytic reaction environment. The color removal efficiency of the spent catalyst was compared to the fresh one in Fig. 10d. The high value of decoloring efficiency (about 99% after 30 min of reaction) confirmed the stability of our materials.

4. Conclusions

This work reported a study over the catalytic performances in CWPO of a representative organic pollutant of the $NiFe_{1.98}RE_{0.02}O_4$ (RE = La, Sm, Gd, Dy) spinel ferrites prepared by sol-gel autocombustion method using maleic acid as fuel for the first time.

XRD patterns and IR spectra confirmed the spinel phase formation by the selected synthesis technique. However, pure spinel compounds were prepared only after heating the samples at higher temperatures ($900\,^{\circ}C$) and for particular chemical compositions (the undoped and samarium doped nickel ferrite). Doping nickel ferrite with rare-earth cations decreased crystallite size, particle size and magnetization, but remarkably increased the catalytic performances.

The best catalytic performance, i.e., 90.6% color removal efficiency after only 15 min of degradation process, with a reaction rate constant about 5 times greater than that of $NiFe_2O_4$, was found for the compound doped with La, mainly explained the smaller ratio particle size to crystallite size. The desirability function approach also confirmed $NiFe_{1.98}La_{0.02}O_4$ as the optimal catalyst for the Orange II dye degradation. The Langmuir-Hinshelwood model revealed a significant contribution of the catalytic chemical decay reaction and a minor contribution of the adsorption phenomena for the removal of dye from aqueous solutions using the produced catalysts.

Acknowledgements

References

[1] F. Stüber, J. Font, A. Fortuny, C. Bengoa, A. Eftaxias, A. Fabregat, Top. Catal. 33 (2005) 3–50.
[2] A.I. Borhan, P. Samoila, V. Hulea, A.R. Iordan, M.N. Palamaru, J. Taiwan Inst. Chem. E 45 (2014) 1655–1660.
[3] F. Martınez, J.A. Melero, J.A. Botas, M.I. Pariente, R. Molina, Ind. Eng. Chem. Res. 46 (2007) 4396–4405.
[4] J.A. Botas, J.A. Melero, F. Martınez, M.I. Pariente, Catal. Today 149 (2010) 334–340.
[5] P. Hu, M. Long, Appl. Catal. B: Environ. 181 (2016) 103–117.
[6] A.L.N. Mota, L.F. Albuquerque, L.T.C. Beltrame, O. Chiavone-Filho, A. Machulek Jr., C.A.O. Nascimento, Braz. J. Pet. Gas 2 (3) (2008) 122–142.
[7] K.H. Kim, S.K. Ihm, J. Hazard. Mater. 186 (2011) 16–34.
[8] M. Kurian, D.S. Nair, J. Environ. Chem. Eng. 2 (2014) 63–69.
[9] S. Perathoner, G. Centi, Top. Catal. 33 (2005) 207–224.
[10] S. Navalon, M. Alvaro, H. Garcia, Appl. Catal. B: Environ. 99 (2010) 1–26.
[11] S.R. Pouran, A.A.A. Raman, W.M.A.W. Daud, J. Clean. Prod. 64 (2014) 24–35.
[12] A.S. Albuquerque, M.V.C. Tolentino, J.D. Ardisson, F.C.C. Moura, R. Mendonca, W.A.A. Macedo, Ceram. Int. 38 (2012) 2225–2231.
[13] A. Xu, M. Yang, R. Qiao, H. Du, C. Sun, J. Hazard. Mater. 147 (2007) 449–456.
[14] S. Jauhar, S. Singhal, M. Dhiman, Appl. Catal. A 486 (2014) 210–218.
[15] P. Samoila, T. Slatineanu, P. Postolache, A.R. Iordan, M.N. Palamaru, Mater. Chem. Phys. 136 (2012) 241–246.
[16] S. Zinatloo-Ajabshir, M. Salavati-Niasari, Z. Zinatloo-Ajabshir, Mater. Lett 180 (2016) 27–30.
[17] Z. Salehi, S. Zinatloo-Ajabshir, M. Salavati-Niasari, RSC Adv. 6 (2016) 26895–26901.
[18] S. Zinatloo-Ajabshir, M. Salavati-Niasari, M. Hamadanian, RSC Adv. 5 (2015) 33792–33800.
[19] S. Zinatloo-Ajabshir, M. Salavati-Niasari, Ceram. Int. 41 (2015) 567–575.
[20] S. Zinatloo-Ajabshir, M. Salavati-Niasari, New J. Chem. 39 (2015) 3948–3955.
[21] S. Zinatloo-Ajabshir, M. Salavati-Niasari, J. Mater. Sci.: Mater. Electron. 26 (2015) 5812–5821.
[22] M. Sadat Morassaei, S. Zinatloo-Ajabshir, M. Salavati-Niasari, J. Mol. Liq. 220 (2016) 902–909.
[23] S. Mortazavi-Derazkola, S. Zinatloo-Ajabshir, M. Salavati-Niasari, Ceram. Int. 41 (2015) 9593–9601.
[24] P. Samoila, L. Sacarescu, A.I. Borhan, D. Timpu, M. Grigoras, N. Lupu, M. Zaltariov, V. Harabagiu, J. Magn. Magn. Mater. 378 (2015) 92–97.
[25] S. Thankachan, M. Kurian, D.S. Nair, S. Xavier, E.M. Mohammed, Int. J. Eng. Sci. Innov. Technol. 3–4 (2014) 529–537.
[26] S. Royer, D. Duprez, F. Can, X. Courtois, C. Batiot-Dupeyrat, S. Laassiri, H. Alamdari, Chem. Rev. 114 (2014) 10292–10368.
[27] F. Ansari, F. Soofivand, M. Salavati-Niasari, Mater. Charact. 103 (2015) 11–17.
[28] S. Mandizadeh, F. Soofivand, M. Salavati-Niasari, S. Bagheri, J. Ind. Eng. Chem. 26 (2015) 167–172.
[29] P. Samoila, C. Cojocaru, I. Cretescu, C.D. Stan, V. Nica, L. Sacarescu, V. Harabagiu, J. Nanomater. ID 713802 (2015).
[30] A.M. Dumitrescu, P.M. Samoila, V. Nica, F. Doroftei, A.R. Iordan, M.N. Palamaru, Powder Technol. 243 (2013) 9–17.
[31] C. Wang, Z. Huang, Mater. Lett. 164 (2016) 194–197.
[32] Z.N. Kayani, M. Butt, Y. Ali, S. Riaz, S. Naseem, Mater. Today: Proc. 2 (2015) 5804–5807.
[33] R.D. Shannon, Acta Cryst. A32 (1976) 751–767.
[34] J. Peng, M. Hojamberdiev, Y. Xu, B. Cao, J. Wang, H. Wu, J. Magn. Magn. Mater. 323 (2011) 133–138.
[35] M. Yehia, S.M. Ismail, A. Hashhash, J. Supercond. Nov. Magn. 27 (2014) 771–774.
[36] D. Carta, M.F. Casula, A. Falqui, D. Loche, G. Mountjoy, C. Sangregorio, A. Corrias, J. Phys Chem. C 113 (2009) 8606–8615.
[37] R. Suresh, K. Giribabu, R. Manigandan, A. Vijayaraj, R. Prabu, A. Stephen, V. Narayanan, J. Iran Chem. Soc. 11 (2014) 645–652.
[38] S. Modak, M. Ammar, F. Mazaleyrat, S. Das, P.K. Chakrabarti, J. Alloys Comp. 473 (2009) 15–19.
[39] M.A. Gabal, S. Kosa, T.S. ElMuttairi, Ceram. Int. 40 (2014) 675–681.
[40] H. Li, Y. Li, L. Xiang, Q. Huang, J. Qiu, H. Zhang, M.V. Sivaiah, F. Baron, J. Barrault, S. Petit, S. Valange, J. Hazard. Mater. 287 (2015) 32–41.
[41] X. Liang, Y. Zhong, S. Zhu, J. Zhu, P. Yuan, H. He, J. Zhang, J. Hazard. Mater. 181 (2010) 112–120.
[42] Z. Binxia, L. Jinchao, L. Linxue, Z. Xiaoli, Z. Yi, S. Tian, Y. Na, Third International Conference on Digital Manufacturing and Automation (ICDMA) (2012) 630–633, http://dx.doi.org/10.1109/ICDMA.2012.149.
[43] F. Luo, D. Yang, Z. Chen, R. Megharaj, R. Naidu, J. Hazard. Mater. 303 (2016) 145–153.
[44] A.I. Borhan, P. Samoila, Vasile Hulea, A.R. Iordan, M.N. Palamaru, J. Photochem. Photobiol. A Chem. 279 (2014) 17–23.
[45] N.R. Costa, J. Lourenco, Z.L. Pereira, Chemometr. Intell. Lab. 107 (2011) 234–244.
[46] M.S. Secula, C.S. Stan, C. Cojocaru, B. Cagnon, I. Cretescu, Sep. Sci. Technol. 49 (2014) 924–938.
[47] K. Vasanth Kumar, K. Porkodi, F. Rocha, Catal. Commun. 9 (2008) 82–84.
[48] C. Betianu, F.A. Caliman, M. Gavrilescu, I. Cretescu, C. Cojocaru, I. Poulios, J. Chem. Technol. Biotechnol. 83 (2008) 1454–1465.